Journal of Nuclear Medicine, published on October 13, 2016 as doi:10.2967/jnumed.116.180299

Predicting response to neoadjuvant chemoradiotherapy in esophageal cancer with textural features derived from pre-treatment ^{18}F-FDG PET/CT imaging

Roelof J. Beukinga MSc[1,2,6] **, Jan B. Hulshoff MD[1], Lisanne V. van Dijk MSc[3], Christina T. Muijs MD PhD[3], Johannes G.M. Burgerhof MSc[4], Gursah Kats-Ugurlu MD[5], Riemer H.J.A. Slart MD PhD[2,6], Cornelis H. Slump PhD[7], Véronique E.M. Mul MD[3], and John Th.M. Plukker MD PhD[1]

[1]Departments of Surgery (Division of Surgical Oncology), University of Groningen, University Medical Center Groningen, Groningen, The Netherlands; [2]Nuclear Medicine and Molecular Imaging, University of Groningen, University Medical Center Groningen, Groningen, The Netherlands; [3]Radiation Oncology, University of Groningen, University Medical Center Groningen, Groningen, The Netherlands; [4]Epidemiology, University of Groningen, University Medical Center Groningen, Groningen, The Netherlands; [5]Pathology, University of Groningen, University Medical Center Groningen, Groningen, The Netherlands; [6]Departments of Biomedical Photonic Imaging, University of Twente, Enschede, The Netherlands; and [7]MIRA Institute for Biomedical Technology and Technical Medicine, University of Twente, Enschede, The Netherlands

** Control over data

Short running title: **Response prediction in esophageal cancer**

Word count: Abstract 327/Manuscript 5422

Conflicts of interest: none

Type of manuscript: Original research

Key words: Textural analysis, response prediction, esophageal cancer, ^{18}F-FDG PET/CT

First author:

Roelof J. Beukinga

PhD fellow Technical Medicine

Department of Biomedical Photonic Imaging

University of Twente, Enschede

Department of Surgery

University of Groningen, University Medical Center Groningen, Groningen

Phone: (00-31) 503612317/ Fax: (00-31) 503614873

E-mail: r.j.beukinga@umcg.nl

Correspondence to:

John Th.M. Plukker MD, PhD

Professor of Surgical Oncology,

Department of Surgery

University of Groningen, University Medical Center Groningen, Groningen

Phone: (00-31) 503612317/ Fax: (00-31) 503614873

E-mail: j.t.m.plukker@umcg.nl

ABSTRACT

Adequate prediction of tumor response to neoadjuvant chemoradiotherapy (nCRT) in esophageal cancer (EC) patients is important in a more personalized treatment. The current best clinical method to predict pathologic complete response is the maximal standardized uptake value (SUV_{max}) in ^{18}F-fluorodeoxyglucose positron emission tomography/computed tomography (^{18}F-FDG PET/CT) imaging. To improve the prediction of response, we constructed a model to predict complete response to nCRT in EC based on pre-treatment clinical parameters and ^{18}F-FDG PET/CT derived textural features. **Methods:** From a prospectively maintained single institution database, we reviewed 97 consecutive patients with locally advanced EC and a pre-treatment ^{18}F-FDG PET/CT between 2009 and 2015. All patients were treated with nCRT (Carboplatin/Paclitaxel/41.4Gy) followed by esophagectomy. We analyzed clinical, geometrical, and pre-treatment textural features extracted from both ^{18}F-FDG PET and CT. Current most accurate prediction model with SUV_{max} as predictor variable was compared with five different response prediction models constructed using Least Absolute Shrinkage and Selection Operator regularized logistic regression. Internal validation was performed to estimate the model's performances. Pathologic response was defined as: complete versus incomplete response (Mandard tumor regression grade system 1 vs. 2-5). **Results:** Pathologic examination revealed 19 (19.6%) complete and 78 (80.4%) incomplete responders. Least Absolute Shrinkage and Selection Operator regularization selected the clinical parameters: histologic type and clinical T-stage, the ^{18}F-FDG PET derived textural feature 'long run low gray level emphasis', and the CT derived textural feature 'run percentage'. Introducing these variables to a logistic regression analysis showed areas under the receiver operating characteristic curve (AUCs) of 0.78 compared to 0.58 in the SUV_{max} model. The discrimination slopes were 0.17 compared to 0.01, respectively. After internal validation, the AUCs decreased to 0.74 and 0.54, respectively.

Conclusion: The predictive values of the constructed models were superior to the standard method (SUV_{max}). These results can be considered as an initial step in predicting tumor response to nCRT in locally advanced EC. Further research in refining the predictive value of these models is needed to justify omission of surgery.

INTRODUCTION

EC is one of the most aggressive tumors with early recurrences even after radical surgery. The standard treatment in locally advanced (T1/N1-3/M0 and T2-4a/N0-3/M0) resectable EC is nCRT followed by a radical esophagectomy. In the Dutch CROSS (ChemoRadiotherapy for Oesophageal cancer followed by Surgery Study) trial, nCRT improved the 5-year overall survival rate from 34% to 47% (*1*). Not all patients benefit from nCRT; 29% of the patients in the CROSS trial had a complete response, 52% had a partial response, and even 18% had no tumor response (*1*). For complete responders, surgical intervention might not be beneficial and a 'wait-and-see policy' might suffice. Hence, adequate response prediction is important in developing personalized treatment in EC. Moreover, accurate response prediction may be relevant in patient counseling in future clinical trial strategies based on personalized treatment. So far, response prediction showed only promising results with functional imaging of tumor viability with ^{18}F-fluorodexoglucose positron emission tomography (^{18}F-FDG PET) and recently with diffusion weighted magnetic resonance imaging (*2-4*). Traditional image-derived indices used in PET rely on quantification of lesion SUVs and overall tumor volume, which have been shown to be important factors for patient outcome and treatment response (*5,6*). Although useful, these parameters omit available information related to the spatial distribution and specific features regarding intra-tumor radiotracer accumulation. This may limit the possibility to further characterize the biological behavior of the tumor, based on hypoxia induced heterogeneity and genomic instability. Intratumoral heterogeneity is correlated with aggressive tumor behavior and a decreased response due to expression of specific receptors with high cellular proliferation and angiogenesis (*7-9*). Hence, even small tumor biopsies, lack complete molecular characterization due to spatially heterogeneity. A novel approach is to quantify spatial heterogeneity of metabolism and tissue density characterized by ^{18}F-FDG uptake and Hounsfield Units with textural features. The concept of textural analysis is based on spatial arrangement of voxels in a predefined volume of interest (VOI). This spatial intratumoral heterogeneity can be depicted from different spatial interrelationships on ^{18}F-FDG PET/CT scans. Therefore, ^{18}F-FDG PET/CT textural features have been proposed to be valuable in response prediction (*10-15*). The aim of this study was to develop a model to predict complete response to nCRT in locally advanced EC based on pre-treatment clinical predictors and ^{18}F-FDG PET/CT derived textural features.

MATERIALS AND METHODS

Patients

In this retrospective study, potentially curatively resectable EC patients were consecutively selected who underwent nCRT followed by esophagectomy between December 2009 and March 2016. Patients with less than 4 courses of chemotherapy, with missing ^{18}F-FDG PET/CT or with incomplete medical records, were excluded, yielding a total of 97 patients. In line with the rules of the Dutch National Health Sciences, our Institutional Review Board approved this retrospective study and the requirement to obtain informed consent was waived.

Data were obtained from a prospectively maintained single institution database including patient characteristics, tumor and treatment related data, and follow-up data. All patients were clinically staged with esophagoscopy and biopsy, endoscopic ultrasonography with fine needle aspiration if indicated, and whole-body integrated ^{18}F-FDG PET/CT. Patients were staged according to the 7th edition of the TNM system maintained by the American Joint Committee on Cancer (*16*) and discussed in the hospital's multidisciplinary esophageal tumor board.

Imaging

PET/CT imaging was performed with an integrated ^{18}F-FDG-PET/CT system (Biograph mCT 4-64 PET/CT, Siemens, Knoxville, TN, USA). Patients fasted for at least 6 hours prior to PET/CT with no restrictions on drinking water. Serum glucose levels were measured before ^{18}F-FDG administration with a weight-based dose of 3 MBq/kg. Sixty minutes after tracer injection, patients were scanned in treatment position. An inspiration breath-hold low-dose CT for attenuation correction was performed, and PET acquisitions were obtained in caudal–cranial direction with field of view 500×500×500 mm, 3D setting, 2-3 min per bed position, matrices of 512 × 512 (0.98 × 0.98 mm pixel size) and 2-mm slice thickness. Image data were reconstructed according to European Association of Nuclear Medicine guidelines (*17*).

Radiotherapy treatment planning including target volume delineation and CT texture analysis was performed on a 16- or 64-multidetector row spiral CT machine (Somatom Sensation 16 or 64; Siemens Medical Systems, Erlangen, Germany). CT thorax/abdomen was obtained in cranial–caudal direction with matrices of 512 × 512 (0.98 × 0.98 mm pixel size) and 3-mm slice thickness.

Treatment and Pathology

Based on the experiences and the good results of the CROSS study, in which our institute had participated, our multidisciplinary tumor board decided to continue nCRT according to the CROSS schedule. This treatment consisted of weekly intravenous administered Paclitaxel (50 mg/m^2) and Carboplatin (AUC 2 $mg \cdot min \cdot mL^{-1}$) during 5 weeks with concurrent external radiotherapy (41.4 Gy in 23 fractions, 5 days per week) (*1*). Transthoracic esophagectomy with two-field lymphadenectomy was performed within 6 to 8 weeks after completion of nCRT. The resected specimens were examined according to a standard protocol (*18*). Resection margins were defined according to the definitions of the College of American Pathologist as microscopic tumor-free (R0: >0mm) or tumor-positive (R1). Pathologic response was assessed by two expert gastrointestinal pathologists according to the Mandard tumor regression grade (TRG) (*19*), ranging from complete response (TRG 1) without viable tumor cells left, to partial response (TRG 2-4) with viable tumor cells left, to no response at all (TRG 5).

Volume of interest

Textural analysis was performed on a VOI incorporating the gross tumor volume for radiation treatment planning. Tumor delineation was performed manually with consensus between three experienced radiation oncologists on axial planes of the radiotherapy planning CT, to enclose three-dimensional coverage of the entire tumor. Involved lymph nodes were not included into the VOI, because these lesions are too small (<10 cm^3) for reliable textural analysis (*20*). The gross tumor volume was rigidly registered to the ^{18}F-FDG PET/CT data series (RTx Workstation 1.0, Mirada Medical, Oxford, UK). Erroneous registrations were manually adjusted after consensus of the collaborating investigators (RJB, CTM, VEM, and JThP).

Tonal discretization

^{18}F-FDG PET/CT imaging data and VOI delineations were loaded into Matlab 2014b (Mathworks, Natick, MA; an interactive image processing environment) for processing and analyses. The SUV, for semi-quantitative analysis of metabolism, was corrected for individual variations in serum glucose level and was discretized to reduce the continuous scale to a finite set of values and to reduce noise throughout the entire study in 0.5 g/mL increments according to Doane's optimal bin width (*21*). Similarly, the Hounsfield unit scale for quantitative analysis of tumor density, was discretized in 30 HU increments for textural analysis.

Candidate predictors

For each patient, a total of 88 parameters were evaluated, including 7 clinical parameters; 16 geometry features; the glycolytic volume based on tumor volume and SUV_{mean}; and 19 first order, 24 second order, and 22 higher order textural features extracted from ^{18}F-FDG PET and CT (supplemental materials). First order textural features are statistics based on the gray level distribution of the image, but do not consider relative positions of gray levels. Second and higher order textural features do consider relative positions of gray levels and therefore allow quantification of heterogeneity. For various spatial interrelationships, frequency distributions (Figure 1) were obtained i.e. the gray level co-occurrence (spatial dependence) matrix for pairwise arrangement of voxels (extracted with a pixel-to-pixel distance equal to 1) (*22*), the gray level run-length matrix for alignment of voxels with the same intensity (*23*), and the gray level size-zone matrix for characteristics of homogenous zones (*24*). Directional voxel analysis was performed in 3 dimensions with a connectivity of 26 voxels and analysis in 13 angular directions. All second and higher order textural features are weighted averages of these matrices to express the relative importance of their properties. All extracted textural features were normalized to the range [0,1].

Statistical analysis

Statistical analysis was performed with R 3.2.2 open-source software using the *glmnet* package (version 2.0-2) and the *rms* package (version 4.4-0), available from the Comprehensive R Archive Network (http://www.r-project.org).

Since textural feature values may be subject to inter-observer variability in the delineation of the tumor, the original delineations were uniformly eroded by ball-shaped structuring elements with radii of 1 and 2 voxels. For each delineation textural features were extracted and the stability of each feature was evaluated with the intra-class correlation (ICC). Only stable features (ICC>0.7) were considered for further analysis. Predictors were then selected by a univariable logistic model with a response variable labeling complete (Mandard TRG 1) and incomplete response (Mandard TRG 2-5). All potential predictors that met the Akaike Information Criterion (AIC) were considered significant. To discourage overfitting, the AIC is based on rewarding goodness-of-fit and penalizing the complexity of the model. The AIC requires $\chi^2 > 2 \cdot df$ i.e. when considering a predictor with one degree of freedom *df*, this implies an $\alpha = P(\chi^2 \geq 2) = 0.157$ (*25*).

Significant predictors were used to construct six multivariable logistic regression models for comparison with current most accurate prediction model with SUV_{max} as predictor variable (model 1). These models were constructed by introducing clinical parameters (model 2); clinical parameters and geometry features (model 3); clinical parameters, geometry features, and PET textural features (model 4); clinical parameters, geometry features, and CT textural features (model 5); and clinical parameters, geometry features, and PET/CT textural features (model 6) to a Least Absolute Shrinkage and Selection Operator, a technique for L1-norm regularization. By increasing the shrinkage parameter λ, the regularization shrinks the estimated coefficients and excludes variables when they become zero. The λ-value that minimized the 10-fold cross validated mean squared error was repeatedly determined with 100 repetitions. The optimal λ-value was robustly determined by averaging over these obtained λ-values. The selected variables were fitted to the data with a logistic regression.

The model's calibration was evaluated using visual inspection of calibration plots and the Hosmer–Lemeshow test. The model's performance was quantified in terms of discrimination with the AUC and the discrimination slope. The goodness-of-fit was evaluated with the -2 log-likelihood and the Nagelkerke R^2. The model was internally validated by a bootstrap approach with 2000 repetitions. Bootstrapping allowed for obtaining the optimism corrected measures for model performance and for shrinkage of the estimated regression coefficients using the optimism-corrected slope.

RESULTS

Patients and treatment

Patient's characteristics are shown in Table 1. Seventy-nine patients (81.4%) received the complete nCRT regimen (all patients received the full radiotherapy dose). Resection with curative intent was performed within a mean time of 56 (standard deviation: 14) days after completion of nCRT. R0 resection was achieved in 90 (92.8%) patients, and R1 resection in seven (7.2%) patients, all with positive circumferential resection margins and one with a positive proximal resection margin. Pathological findings revealed complete response in 19 patients (19.6%) and incomplete response in 78 patients (80.4%).

Model development

For the preselection, 144 of the 147 (97.3%) variables were found to be robust for contour variations. These variables were introduced to univariable logistic regression analysis, resulting in 24 significant variables predictive for response, including 4 clinical parameters; 0 geometry features; 1 first order, 8 second, and 5 higher order PET textural features; and 1 first, 1 second, and 4 higher order CT textural features. All constructed prediction models performed significantly better than model 1 (based on SUV_{max}). Introduction of only significant clinical parameters to the Least Absolute Shrinkage and Selection Operator regularization process, resulted in the selection of histologic type and clinical T-stage (model 2). These variables were selected in each subsequently constructed model. Compared to model 1, the AUC improved from 0.58 to 0.71, the discrimination slope improved from 0.01 to 0.14, and the AIC decreased (ΔAIC = 10.66). For model 3, no additional variables were selected compared to model 2, since no geometry features were significant at the univariable logistic regression analysis. For model 4, the

PET textural feature 'long run low gray level emphasis (LRLGLe-PET)' was selected. Adding this variable did slightly improve the discrimination and the likelihood compared to model 2 and 3, but resulted in a higher AIC (ΔAIC = -0.79). After internal validation, the AUC was equal to 0.69. For model 5, the CT textural feature 'run percentage (RP-CT)' was selected. Although the AIC was almost equal compared to model 2 and 3 (ΔAIC = -0.02), adding this variable improved the discrimination slope to 0.16 and the AUC remarkably to 0.79. This also persisted after internal validation (AUC=0.76). Finally, entering all variables to the modeling process resulted in the selection of all above mentioned variables (model 6). Model 6 had the best goodness-of-fit, but not the lowest AIC (ΔAIC = -0.23, 0.56, and -0.21 compared to models 2 and 3, 4, and 5, respectively). The AUC slightly decreased to 0.78, while the discrimination slope was increased to 0.17. After internal validation, the AUC decreased to 0.74. The model regression coefficients and the corresponding model performance measures are shown in Table 2 and Table 3, respectively. Figure 2 gives the values of the selected textural features and their corresponding frequency distributions for a complete and a non-responder. For the selected textural features, the range of values to reproduce the normalization process and the found ICCs for quantifying contouring robustness are given in (supplemental materials).

DISCUSSION

An adequate method to predict pathologic complete response after nCRT has not yet been defined in EC patients. In personalized treatment, accurate response prediction will lead to a paradigm shift with omitting surgical treatment in complete responders or preventing unnecessary nCRT in non-responders. Response evaluation of nCRT is commonly based on tumor metabolic response measured by SUV_{max} with ^{18}F-FDG PET, but with a low sensitivity and specificity of 67% and 68%, respectively (*26*). Current study is the first in predicting complete response with ^{18}F-FDG-PET/CT derived textural features in a homogeneous group of EC patients treated according to the CROSS regimen. We demonstrated that all constructed prediction models showed significant improvement compared to predictions based on SUV_{max} alone and may therefore be considered as an initial step in predicting response.

In this study, the most predictive textural features were LRLGLe-PET and RP-CT. LRLGLe-PET depends on long runs (coarse texture) with low gray levels and was higher (i.e. low and homogeneous ^{18}F-FDG uptake) for complete responders and lower (i.e. high and heterogeneous ^{18}F-FDG uptake) for incomplete responders, possibly due to tumor hypoxia and necrosis. RP-CT measures the homogeneity of runs (fine texture) and was higher in complete responders. In univariable logistic regression, high LRLGLe-PET and RP-CT values were associated with squamous cell carcinoma (P=0.12 and P=0.13, respectively), confirming the higher complete response rates in squamous cell carcinoma (*1*).

The clinical value of SUV_{max} was limited, possibly because it is extracted from a single voxel and does not characterize the total ^{18}F-FDG uptake. This causes a high dependency on the quality of the PET images (including noise) and the voxel size, which induces a low reproducibility.

Several studies focused on response prediction in EC using ^{18}F-FDG PET/CT derived textural features (Table 4). Van Rossum et al. concluded that ^{18}F-FDG PET derived textural features provide statistical value (*14*), but this does not translate into a clinically relevant benefit, which is in line with our findings. They only performed ^{18}F-FDG PET textural analysis, while this study demonstrates the additional value of CT textural analysis. Other studies demonstrated promising findings, but are hampered by several limitations, including small patient cohorts with heterogeneous treatment schedules, lack of multivariable analyses, and a substantial chance of model overfitting due to the lack of optimism correction (*11-13,15*).

A limitation of this study is the absence of external validation, which is essential for implementation into clinical practice. Moreover, several factors should be considered which affect textural analysis: (a) Changing the bin width influences the quantization noise and has a crucial effect on textural features (*27*). Although only an indication, we used Doane's optimal bin width to discretize the SUVs and Hounsfield Units (*21*). (b) Respiratory gated PET/CT acquisitions could be considered to reduce respiration-induced smearing and contrast degradation (*28*).

The constructed prediction model may serve as a basic model, which can be extended with new features for usage for other applications. Current constructed model might be helpful towards a safe decision in postponing a burdensome surgical procedure in patients with a doubtful adequate physical condition after nCRT. In patients treated with definitive chemoradiotherapy detection of non-responders might allow additional treatments when available, while in complete responders an adjusted follow-up might be justified, to identify candidates for salvage surgery.

Up to now, the authors do not consider the predictive value of the constructed model high enough to justify the omission of surgery after nCRT in EC. A potential approach to improve the constructed basic prediction models could be: (a) Adding interim- or post-treatment textural analysis. Studies investigating both pre- and post-treatment textural analysis mainly reported post-treatment textural features to be associated with response (*12,14,15*). We performed a post-treatment textural analysis in patients with a post-treatment PET/CT scan (n=20), and found 21 significant textural features for response in univariable regression analysis. However, post-treatment textural analysis suffers from radiation induced esophagitis which complicates delineation of the primary tumor and difficulties in "tumor" delineation in complete responders. (b) Texture could be characterized with more specific PET tracers like ^{18}F-fluoroerythronitroimidazole (^{18}F-FETNIM; quantifying hypoxia) (*29*) or ^{18}F-fluorothymidine (^{18}F-FLT; targeting cellular proliferation) (*30*) or by other functional imaging modalities including the apparent diffusion coefficient (ADC) in diffusion weighted magnetic resonance imaging (*4*). (c) Biological markers have shown to be potential molecular markers in individualizing EC treatment and may be incorporated to improve prediction models (*31*).

CONCLUSION

The constructed models are a valuable initial step in predicting response to nCRT in locally advanced EC. Adding the ^{18}F-FDG PET derived textural feature 'long run low gray level emphasis' and the CT derived textural feature 'run percentage' to a model with the clinical parameters histologic type and clinical T-stage, is potentially predictive and was more accurate than response prediction based on SUV_{max}. These models may serve as basic models in determining clinical complete responders and can be extended with new features for usage for other applications.

DISCLOSURE

None of the authors have any financial or other relationship that could be construed as a conflict of interest.

REFERENCES

1. van Hagen P, Hulshof MC, van Lanschot JJ, et al. Preoperative chemoradiotherapy for esophageal or junctional cancer. *N Engl J Med.* 2012;366:2074-2084.

2. Chen YM, Pan XF, Tong LJ, Shi YP, Chen T. Can ^{18}F-fluorodeoxyglucose positron emission tomography predict responses to neoadjuvant therapy in oesophageal cancer patients? A meta-analysis. *Nucl Med Commun.* 2011;32:1005-1010.

3. Ott K, Weber WA, Lordick F, et al. Metabolic imaging predicts response, survival, and recurrence in adenocarcinomas of the esophagogastric junction. *J Clin Oncol.* 2006;24:4692-4698.

4. van Rossum PS, van Lier AL, van Vulpen M, et al. Diffusion-weighted magnetic resonance imaging for the prediction of pathologic response to neoadjuvant chemoradiotherapy in esophageal cancer. *Radiother Oncol.* 2015;115:163-170.

5. Boggs DH, Hanna A, Burrows W, Horiba N, Suntharalingam M. Primary gross tumor volume is an important prognostic factor in locally advanced esophageal cancer patients treated with trimodality therapy. *J Gastrointest Cancer.* 2015;46:131-137.

6. Pan L, Gu P, Huang G, Xue H, Wu S. Prognostic significance of SUV on PET/CT in patients with esophageal cancer: a systematic review and meta-analysis. *Eur J Gastroenterol Hepatol.* 2009;21:1008-1015.

7. Diaz-Cano SJ. Tumor heterogeneity: mechanisms and bases for a reliable application of molecular marker design. *Int J Mol Sci.* 2012;13:1951-2011.

8. Harris AL. Hypoxia--a key regulatory factor in tumour growth. *Nat Rev Cancer.* 2002;2:38-47.

9. Rajendran JG, Schwartz DL, O'Sullivan J, et al. Tumor hypoxia imaging with [F-18] fluoromisonidazole positron emission tomography in head and neck cancer. *Clin Cancer Res.* 2006;12:5435-5441.

10. Chicklore S, Goh V, Siddique M, Roy A, Marsden PK, Cook GJ. Quantifying tumour heterogeneity in ^{18}F-FDG PET/CT imaging by texture analysis. *Eur J Nucl Med Mol Imaging.* 2013;40:133-140.

11. Hatt M, Tixier F, Cheze Le Rest C, Pradier O, Visvikis D. Robustness of intratumour ^{18}F-FDG PET uptake heterogeneity quantification for therapy response prediction in oesophageal carcinoma. *Eur J Nucl Med Mol Imaging.* 2013;40:1662-1671.

12. Tan S, Kligerman S, Chen W, et al. Spatial-temporal [^{18}F]FDG-PET features for predicting pathologic response of esophageal cancer to neoadjuvant chemoradiation therapy. *Int J Radiat Oncol Biol Phys.* 2013;85:1375-1382.

13. Tixier F, Le Rest CC, Hatt M, et al. Intratumor heterogeneity characterized by textural features on baseline ^{18}F-FDG PET images predicts response to concomitant radiochemotherapy in esophageal cancer. *J Nucl Med.* 2011;52:369-378.

14. van Rossum PS, Fried DV, Zhang L, et al. The incremental value of subjective and quantitative assessment of ^{18}F-FDG PET for the prediction of pathologic complete response to preoperative chemoradiotherapy in esophageal cancer. *J Nucl Med.* 2016;57:691-700.

15. Zhang H, Tan S, Chen W, et al. Modeling pathologic response of esophageal cancer to chemoradiation therapy using spatial-temporal ^{18}F-FDG PET features, clinical parameters, and demographics. *Int J Radiat Oncol Biol Phys.* 2014;88:195-203.

16. Edge SB, Compton CC. The American Joint Committee on Cancer: the 7th edition of the AJCC cancer staging manual and the future of TNM. *Ann Surg Oncol.* 2010;17:1471-1474.

17. Boellaard R, O'Doherty MJ, Weber WA, et al. FDG PET and PET/CT: EANM procedure guidelines for tumour PET imaging: version 1.0. *Eur J Nucl Med Mol Imaging.* 2010;37:181-200.

18. Muijs C, Smit J, Karrenbeld A, et al. Residual tumor after neoadjuvant chemoradiation outside the radiation therapy target volume: a new prognostic factor for survival in esophageal cancer. *Int J Radiat Oncol Biol Phys.* 2014;88:845-852.

19. Mandard AM, Dalibard F, Mandard JC, et al. Pathologic assessment of tumor regression after preoperative chemoradiotherapy of esophageal carcinoma. Clinicopathologic correlations. *Cancer.* 1994;73:2680-2686.

20. Hatt M, Majdoub M, Vallieres M, et al. ^{18}F-FDG PET uptake characterization through texture analysis: investigating the complementary nature of heterogeneity and functional tumor volume in a multi-cancer site patient cohort. *J Nucl Med.* 2015;56:38-44.

21. Doane DP. Aesthetic frequency classifications. *The American Statistician.* 1976;30:181-183.

22. Haralick RM, Shanmugam K, Dinstein I. Textural features for image classification. *IEEE Transactions on Systems, Man, and Cybernetics.* 1973;3:610-621.

23. Galloway MM. Texture analysis using gray level run lengths. *Computer Graphics and Image Processing.* 1975;4:172-179.

24. Thibault G, Angulo J, Meyer F. Advanced Statistical Matrices for Texture Characterization: Application to Cell Classification. *IEEE Transactions on Biomedical Engineering.* 2014;61:630-637.

25. Akaike H. A new look at the statistical model identification. *IEEE Transactions on Automatic Control.* 1974;19:716-723.

26. Kwee RM. Prediction of tumor response to neoadjuvant therapy in patients with esophageal cancer with use of ^{18}F FDG PET: a systematic review. *Radiology.* 2010;254:707-717.

27. Leijenaar RT, Nalbantov G, Carvalho S, et al. The effect of SUV discretization in quantitative FDG-PET Radiomics: the need for standardized methodology in tumor texture analysis. *Sci Rep.* 2015;5:11075.

28. Sindoni A, Minutoli F, Pontoriero A, Iati G, Baldari S, Pergolizzi S. Usefulness of four dimensional (4D) PET/CT imaging in the evaluation of thoracic lesions and in radiotherapy planning: Review of the literature. *Lung Cancer.* 2016;96:78-86.

29. Yue J, Yang Y, Cabrera AR, et al. Measuring tumor hypoxia with ^{18}F-FETNIM PET in esophageal squamous cell carcinoma: a pilot clinical study. *Dis Esophagus.* 2012;25:54-61.

30. Yue J, Chen L, Cabrera AR, et al. Measuring tumor cell proliferation with ^{18}F-FLT PET during radiotherapy of esophageal squamous cell carcinoma: a pilot clinical study. *J Nucl Med.* 2010;51:528-534.

31. Honing J, Pavlov KV, Mul VE, et al. CD44, SHH and SOX2 as novel biomarkers in esophageal cancer patients treated with neoadjuvant chemoradiotherapy. *Radiother Oncol.* 2015;117:152-158.

32. Therasse P, Arbuck SG, Eisenhauer EA, et al. New guidelines to evaluate the response to treatment in solid tumors. European Organization for Research and Treatment of Cancer, National Cancer Institute of the United States, National Cancer Institute of Canada. *J Natl Cancer Inst.* 2000;92:205-216.

33. Chirieac LR, Swisher SG, Ajani JA, et al. Posttherapy pathologic stage predicts survival in patients with esophageal carcinoma receiving preoperative chemoradiation. *Cancer.* 2005;103:1347-1355.

FIGURE LEGENDS

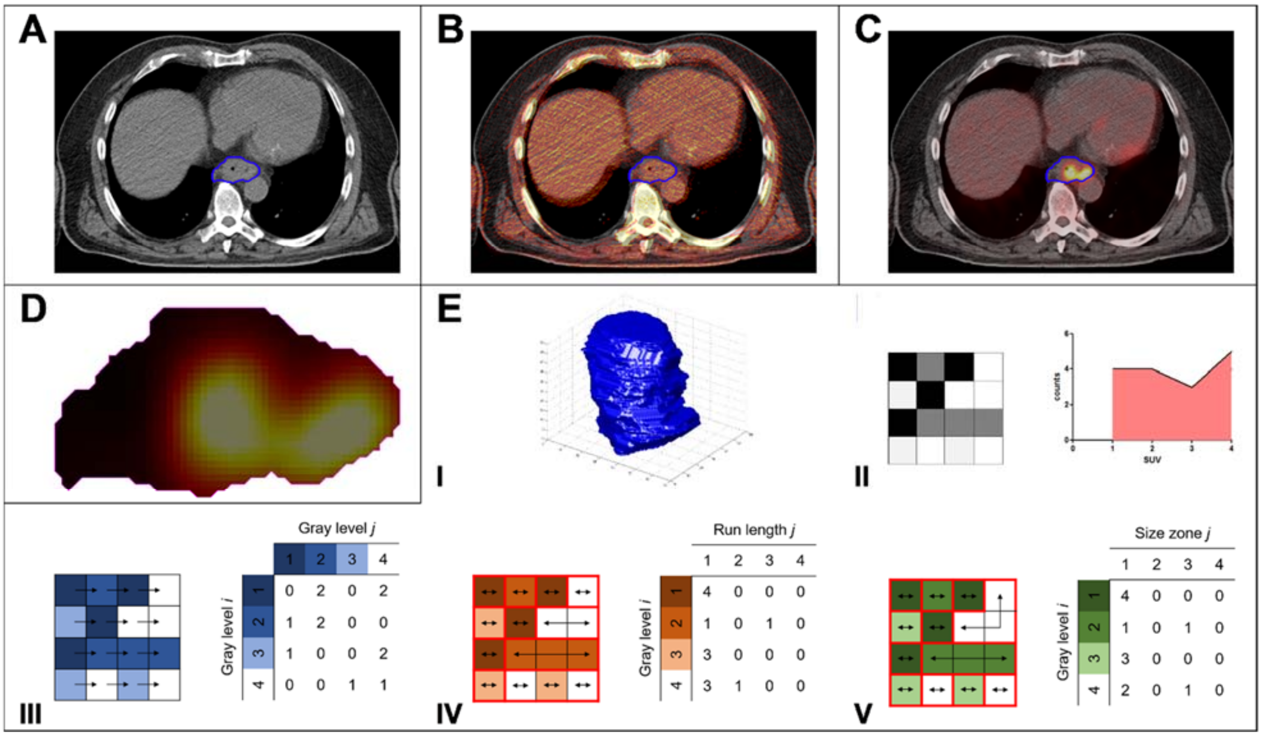

FIGURE 1: A) Manual delineation of the gross tumor volume on planning CT; B) Co-registration of LD-CT (lava colormap) to the radiotherapy planning CT (grayscale colormap); C) Overlay of PET image (lava colormap) onto radiotherapy planning CT (grayscale colormap); D) Cropping of PET VOI; E) Feature extraction; I) Assessment of tumor shape by means of geometry features; II) Global assessment of tonal distribution by means of first order textural features; III) Assessment of pairwise arrangement of voxels by means of grey level co-occurrence matrix; IV) Assessment of alignment of voxels with the same intensity by means of grey level run-length matrix; V) Assessment of characteristics of homogenous zones by means of grey level size-zone matrix.

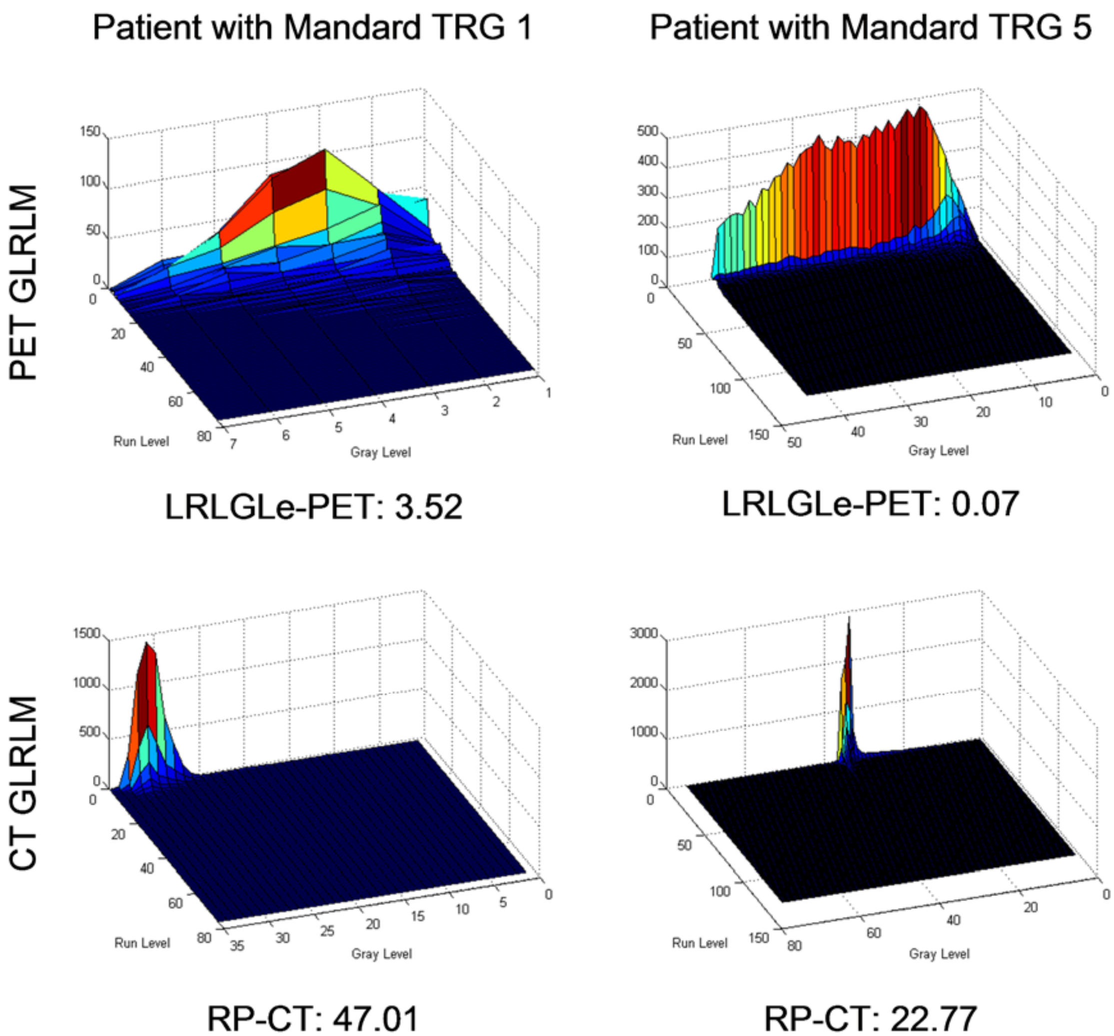

FIGURE 2: Example of the values of the selected textural features and their corresponding frequency distributions for a complete and a non-responder.

Abbreviations: GLRLM: gray level run-length matrix; LRLGLe-PET: long run low gray level emphasis measured on PET; and RP-CT: run percentage measured on CT.

TABLES

TABLE 1: Patient's characteristics.

Characteristic		N	%	Characteristic		N	%
Gender	Male	82	84.5	cN stage	cN0	21	21.7
	Female	15	15.5		cN1	45	46.4
Age	<70 y	78	80.4		cN2	28	28.9
	≥70 y	19	19.6		cN3	3	3.1
Histology	AC	88	90.7	ypT stage	ypT0	19	19.6
	SCC	9	9.3		ypT1	13	13.4
Tumor grade	Missing	6	6.2		ypT2	13	13.4
	G1	49	50.5		ypT3	52	53.6
	G3	42	43.3	ypN stage	ypN0	63	65.0
EUS tumor length	<5 cm	37	40.2		ypN1	18	18.6
	≥5 cm	58	59.8		ypN2	10	10.3
Localization	Mid	4	4.1		ypN3	6	6.2
	Distal	62	63.9	CRM*	R0	90	92.8
	GEJ	31	32.0		R1	7	7.2
nCRT cycles	4	18	18.6	Proximal resection margin*	R0	96	99.0
	5	79	81.4		R1	1	1.0
cT stage	cT1	2	2.1	Mandard TRG	1	19	19.6
	cT2	16	16.5		2	23	23.7
	cT3	74	76.3		3	37	38.1
	cT4a	5	5.2		4	15	15.5
					5	3	3.1

* Tumor-free (R0) resection margin defined according to criteria of the CAP as >0mm.

Abbreviations: AC: adenocarcinoma; SCC: squamous cell carcinoma; EUS: endoscopic ultrasonography; GEJ: gastresophageal junction; nCRT: neoadjuvant chemoradiotherapy; TRG: tumor regression grade; cT/N: clinical tumor/nodal stage; ypT/N: pathologic tumor/nodal stage after nCRT; and CAP: College of American Pathologists.

TABLE 2: Estimated regression coefficients of the prediction models for pathologic complete response without optimism correction.

	Model 1			Model 2 – 3			Model 4			Model 5			Model 6		
Variable	Coef.	S.E.	p	Coef.	S.E.	P	Coef.	S.E.	p	Coef.	S.E.	p	Coef.	S.E.	p
Intercept	-0.88	0.50	0.08	-0.42	0.50	0.39	-0.86	0.65	0.19	-1.15	0.72	0.11	-1.83	0.91	0.04
SUV_{max}	-1.72	1.45	0.24												
Histology															
AC				1.00			1.00			1.00			1.00		
SCC				-1.70	0.61	0.01	-1.47	0.65	0.02	-1.89	0.64	0.00	-1.63	0.67	0.02
cT stage															
cT1 & cT2				1.00			1.00			1.00			1.00		
cT3 & cT4a				2.03	0.78	0.01	1.98	0.80	0.01	2.27	0.81	0.00	2.23	0.83	0.01
LRLGLe-PET							0.56	0.55	0.31				0.71	0.59	0.23
RP-CT										0.01	0.01	0.15	0.02	0.01	0.10

Abbreviations: LRLGLe-PET: long run low gray level emphasis measured on PET; and RP-CT: run percentage measured on CT.

TABLE 3: Estimates of model performance for the four prediction models.

	Goodness-of-fit			Discrimination		Calibration			Validation	
	-2LLH	AIC	R^2	AUC	DS	Intercept	Slope	HLp	R^2 boot	AUC boot
Model 1	94.46	98.46	0.02	0.58	0.01	2.09	2.46	0.75	0.00	0.54
Model 2 – 3	81.80	87.80	0.22	0.71	0.14	-0.04	0.94	1.00	0.17	0.70
Model 4	80.59	88.59	0.23	0.71	0.15	-0.15	0.87	0.45	0.17	0.69
Model 5	79.82	87.82	0.24	0.79	0.16	-0.14	0.86	0.42	0.18	0.76
Model 6	78.03	88.03	0.27	0.78	0.17	-0.22	0.81	0.46	0.18	0.74

Abbreviations: -2LLH: -2 log-likelihood; AIC: Akaike information criterion; R^2: Nagelkerke R^2; AUC: area under the receiver operating characteristic; DS: discrimination slope; HLp: Hosmer–Lemeshow p-value; and boot: internal validated with bootstrapping.

TABLE 4: Current literature describing [18]F-FDG PET texture analysis in response prediction in EC.

Study	n	Type	nCRT	Timing PET/CT	Outcome	Reported entered variables
Tixier et al. (*13*)	41	AC, SCC	60 Gy + Cisplatin or Carboplatin/Fluorouracil	Pre-nCRT	CR vs. PR vs. NR (*32*)	Pre Local homogeneity Pre Local entropy Pre Coarseness Pre Intensity variability Pre Size-zone features
Hatt et al. (*11*)	50	AC, SCC	60 Gy + Cisplatin / Fluorouracil	Pre-nCRT	CR + PR vs. NR (*32*)	Pre MATV Pre Entropy Pre Homogeneity Pre Dissimilarity Pre Intensity variability Pre Zone percentage
Tan et al. (*12*)	20	AC, SCC	50.4 Gy + Cisplatin / Fluorouracil	Pre- and post-nCRT	TRG 1+2 vs. 3-5 (*19*)	ΔSUV_{max} SUV_{max} ratio ΔSUV_{mean} Pre Skewness Post Inertia Post Correlation Post Cluster prominence
Zhang et al. (*15*)	20	AC, SCC	50.4 Gy + Cisplatin or Carboplatin	Pre- and post-nCRT	TRG 1+2 vs. 3-5 (*19*)	Post Orientation Tumor involves GEJ ΔInertia Post Energy Post Entropy ΔSkewness
Van Rossum et al. (*14*)	217	AC	45 or 50.4 Gy + Fluoropyrimidine with either a platinum compound or a taxane	Pre- and post-nCRT	TRG 1 vs. 2-4 (*33*)	EUS tumor length cT stage Induction chemotherapy Post nCRT endoscopic biopsy Subjective PET assessment Post nCRT TLG Pre Cluster shade ΔRun percentage ΔGLCM Entropy Post nCRT Roundness
Current study	97	AC, SCC	41.4 Gy + Carboplatin/ Paclitaxel	Pre-nCRT	TRG 1 vs. 2-5 (*19*)	Histology cT stage Pre LRLGLe-PET Pre RP-CT

Abbreviations: AC: adenocarcinoma; SCC: squamous cell carcinoma; TRG: tumor response grade; nCRT: neoadjuvant chemoradiotherapy; MATV: metabolically active tumor volume; SUV: standardized uptake value; GEJ: gastroesophageal junction; EUS: endoscopic ultrasonography; cT: clinical T-stage; TLG: total lesion glycolysis; GLCM: grey level co-occurrence matrix; LRLGLe-PET: long run low gray level emphasis measured on PET; and RP-CT: run percentage measured on CT.

Range of values and ICCs for quantifying contouring robustness for the selected textural features.

Variable	Min	Max	ICC Estimate	ICC Lower	ICC Upper
LRLGLe-PET	0.02	4.21	0.95	0.93	0.96
RP-CT	12.05	153.76	0.93	0.91	0.95

Abbreviations: LRLGLe-PET: long run low gray level emphasis measured on PET; and RP-CT: run percentage measured on CT.

Geometry features

Variable	Equation	Description
Volume	N/A	Volume.
Surface area	N/A	Total surface area.
Boundingbox volume	N/A	The smallest cubic volume containing the volume of interest.
Extent	P01/P03	The volume to boundingbox ratio.
Major axis length	N/A	The length of the major axis.
Minor axis length	N/A	The length of the minor axis.
Flattening	$\frac{\mathrm{P05} - \mathrm{P06}}{\mathrm{P05}}$	A measure of how much the symmetry axis is compressed relative to the equatorial radius.
Aspect ratio	P06/P05	The minor axis length to the major axis length ratio.
Sphericity	$\frac{\pi^{\frac{1}{3}} \cdot (6 \cdot P01)^{\frac{2}{3}}}{P02}$	A measure of how spherical (round) an object is.
Convex area	N/A	Area of smallest convex polygon that contains the volume of interest.
Solidity	P01/P10	The volume to convex area ratio.
Equivalent diameter	$\left(\frac{6 \cdot P01}{\pi}\right)^{\frac{1}{3}}$	The diameter of a circle with the same area as the region.
Spherical disproportion	$\frac{P02}{4\pi R^2}$	A measure of surface regularity, indicating how close the shape is to a sphere.
Surface to volume ratio	P02/P01	The surface to volume ratio.
Compactness 1	$\frac{P01}{\sqrt{\pi} A^{\frac{2}{3}}}$	The degree to which a shape is compact. The most compact shape is a perfect sphere.
Compactness 2	$\frac{36\pi \cdot P01^2}{A^3}$	The degree to which a shape is compact. The most compact shape is a perfect sphere.

Total glycolytic volume

Variable	Equation	Description
Total glycolytic volume	Volume · Mean intensity	The total lesion volume and its metabolic activity.

First order texture features

Notation:

I	The intensity values of the three dimensional image matrix with N voxels.
P	The first order histogram with N_l discrete intensity levels.

Variable	Equation	Description
Minimum	N/A	Minimum intensity.
Maximum	N/A	Maximum intensity.
Range	Maximum - minimum	Intensity range.
Mean	$\mu = \frac{\sum I}{N}$	Mean intensity.
Quantile 0.025	N/A	Intensity of the 0.025 quantile.
Quantile 0.25	N/A	Intensity of the 0.25 quantile.
Median intensity	N/A	Median intensity.
Quantile 0.75	N/A	Intensity of the 0.75 quantile.
Quantile 0.975	N/A	Intensity of the 0.975 quantile.
Sum intensity	$\sum I$	Sum of all intensities.
Variance	$\frac{1}{N-1}\sum (I-\mu)^2$	Variance.
SD	$\sqrt{\frac{1}{N-1}\sum (I-\mu)^2}$	Standard deviation.
Skewness	$\frac{\frac{1}{N}\sum(I-\mu)^3}{\left(\sqrt{\frac{1}{N}\sum(I-\mu)^2}\right)^3}$	A measure of the asymmetry of the data around the sample mean.
Kurtosis	$\frac{\frac{1}{N}\sum(I-\mu)^4}{\left(\sqrt{\frac{1}{N}\sum(I-\mu)^2}\right)^2}$	A measure of how outlier-prone a distribution is.
Energy	$\sum I^2$	The summation of all squared intensities.
Entropy	$\sum_{i=1}^{Nl} P(i)\log_2 P(i)$	A measure of randomness, which is largest for random grey level distributions.
Mean absolute deviation	$\sum \lvert I-\mu \rvert$	The mean of the absolute deviations of all voxel intensities around the mean intensity value.
RMS	$\frac{\sqrt{\sum I^2}}{N}$	Root mean square.
Uniformity	$\sum_{i=1}^{N_l} P(i)^2$	A measure of how uniform a distribution is.

GLCM-based second order textural features

Notation:

$GLCM(i,j)$	(i,j)th entry in a normalized GLCM.
N_g	Number of distinct grey levels in the quantized image.
$\sum_i GLCM(i,j)$ and $\sum_j GLCM(i,j)$	$\sum_{i=1}^{N_g} GLCM(i,j)$ and $\sum_{j=1}^{N_g} GLCM(i,j)$
$GLCM_x(i)$ and $GLCM_y(j)$	$\sum_j GLCM(i,j)$ and $\sum_i GLCM(i,j)$
$GLCM_{x+y}(k), \quad i+j=k$	$\sum_i \sum_j GLCM(i,j), k=2,3,\ldots,2N_g$
$GLCM_{x-y}(k), \quad \lvert i-j \rvert=k$	$\sum_i \sum_j GLCM(i,j), k=0,1,\ldots,N_g-1$
μ_x and μ_y	The mean of $GLCM_x(i)$ and $GLCM_y(j)$
σ_x and σ_y	The standard deviation of $GLCM_x(i)$ and $GLCM_y(j)$
HX	$-\sum_i GLCM_x(i)\log_2[GLCM_x(i)]$, the entropy of $GLCM_x$
HY	$-\sum_i GLCM_y(j)\log_2[GLCM_y(j)]$, the entropy of $GLCM_y$
HXY	$-\sum_i \sum_j GLCM(i,j)\log_2[GLCM(i,j)]$
$HXY1$	$-\sum_i \sum_j GLCM(i,j)\log_2[GLCM_x(i)\cdot GLCM_y(j)]$
$HXY2$	$-\sum_i \sum_j GLCM_x(i)\cdot GLCM_y(j)\log_2[GLCM_x(i)\cdot GLCM_y(j)]$

Variable	Equation	Description
Autocorrelation	$\sum_i \sum_j (i\cdot j)GLCM(i,j)$	A measure of coarseness.
Contrast (inertia)	$\sum_i \sum_j \lvert i-j \rvert^2 GLCM(i,j)$	A measure of local variations present in the image. A high contrast value indicates a high degree of local variation.
Correlation	$\sum_i \sum_j \frac{(i-\mu_x)(j-\mu_y)GLCM(i,j)}{\sigma_x\sigma_y}$	A measure of grey tone linear dependency of neighbouring cells. For an image with large areas of similar intensities, correlation is higher than for an image with noisier, uncorrelated intensities.
Haralick's correlation	$\sum_i \sum_j \frac{(i\cdot j)GLCM(i,j)-\mu_x\mu_y}{\sigma_x\sigma_y}$	A measure of how correlated a voxel is to its neighbour.
Cluster prominence	$\sum_i \sum_j (i+j-\mu_x-\mu_y)^4 GLCM(i,j)$	A measure of local intensity variation.
Cluster shade	$\sum_i \sum_j (i+j-\mu_x-\mu_y)^3 GLCM(i,j)$	A measure of the lack of symmetry of the matrix. High values represent asymmetric matrices.
Cluster tendency	$\sum_i \sum_j (i+j-\mu_x-\mu_y)^2 GLCM(i,j)$	Indicates into how many clusters the grey levels can be classified.
Dissimilarity	$\sum_i \sum_j \lvert i-j \rvert GLCM(i,j)$	A measure that defines the variation of grey level pairs.
Energy (Angular second moment)	$\sum_i \sum_j GLCM(i,j)^2$	Emphasizes local homogeneity. Homogeneous images have few dominant grey tone transitions, which results into a higher energy.
Entropy	$-\sum_i \sum_j GLCM(i,j)\cdot\log_2(GLCM(i,j))$	A measure of disorder. When the image is not texturally uniform, entropy is very large.
Homogeneity 1	$\sum_i \sum_j \frac{GLCM(i,j)}{1+\lvert i-j \rvert}$	A measure of local homogeneity, which measures the closeness of the distribution of elements in the GLCM to the GLCM diagonal; high values indicate smooth texture with low variation.
Homogeneity 2	$\sum_i \sum_j \frac{GLCM(i,j)}{1+\lvert i-j \rvert^2}$	A measure of local homogeneity, which measures the closeness of the distribution of elements in the GLCM to the GLCM diagonal; high values indicate smooth texture with low variation.
Maximum probability	$\max_{i,j} GLCM(i,j)$	Determines the grey level with the maximum probability in the GLCM. The maximum probability is expected to be high if the occurrence of the most predominant voxel pair is high.
Sum of squares: variance	$\sum_i \sum_j (i-\mu)^2 GLCM(i,j)$	A measure of heterogeneity, which characterizes the distribution of grey levels around the mean. This feature

		puts relatively high weights on the elements that differ from the average value of the GLCM.
Sum average	$\sum_{i=2}^{2N_g} i \cdot GLCM_{x+y}(i)$	A measure of the relation between clear and dense areas in an image.
Sum entropy	$-\sum_{i=2}^{2N_g} GLCM_{x+y}(i) \cdot \log(GLCM_{x+y}(i))$	Entropy of the sum histogram.
Sum variance	$-\sum_{i=2}^{2N_g} (i - \text{Sum entropy})^2 \cdot GLCM_{x+y}(i)$	Variance of the sum histogram.
Difference variance 1	$\sum_{i=0}^{N_g-1} i^2 \cdot GLCM_{x-y}(i)$	Variance of the difference histogram.
Difference variance 2	$\frac{1}{N_g - 1}\sum_i \sum_j (GLCM(i,j) - \mu)^2$	Variance of the difference histogram.
Difference entropy	$-\sum_{i=0}^{N_g-1} GLCM_{x-y}(i) \cdot \log(GLCM_{x-y}(i)$	Entropy of the difference histogram.
Information measure of correlation 1	$\frac{HXY - HXY1}{\max(HX, HY)}$	This measure is a function of the joint probability density distribution $p(x,y)$ of the two variables x and y, and is invariant under a change of parameterization $x' = f(x)$, $y' = g(y)$, and reduces to the classical correlation coefficient when $p(x, y)$ is normal.
Information measure of correlation 2	$\sqrt{1 - e^{-2(HXY2 - HXY)}}$	This measure is a function of the joint probability density distribution $p(x,y)$ of the two variables x and y, and is invariant under a change of parameterization $x' = f(x)$, $y' = g(y)$, and reduces to the classical correlation coefficient when $p(x, y)$ is normal.
Inverse difference normalized	$\sum_i \sum_j \frac{GLCM(i,j)}{1 + \frac{\lvert i-j \rvert^2}{N_g}}$	A measure of image local homogeneity as it assumes larger values for smaller grey tone differences in pair elements. It is more sensitive to the presence of near diagonal elements in the GLCM.
Inverse difference moment normalized	$\sum_i \sum_j \frac{GLCM(i,j)}{1 + \frac{(i-j)^2}{N_g}}$	A measure of image local homogeneity as it assumes larger values for smaller grey tone differences in pair elements. It is more sensitive to the presence of near diagonal elements in the GLCM.

GLRLM-based second order textural features.

Notation:

$GLRLM(i,j)$	(i,j)th entry in a GLRLM.
$\sum_i GLRLM(i,j)$ and $\sum_j GLRLM\,(i,j)$	$\sum_{i=1}^{M} GLRLM(i,j)$ and $\sum_{j=1}^{N} GLRLM\,(i,j)$
n_r	$\sum_i \sum_j GLRLM(i,j)$
n_p	$\sum_i \sum_j j \cdot GLRLM(i,j)$

Variable	Equation	Description
Short Run Emphasis	$\frac{1}{n_r}\sum_i \sum_j \frac{GLRLM(i,j)}{j^2}$	Is highly dependent on the occurrence of short runs and is expected large for fine textures.
Long Run Emphasis	$\frac{1}{n_r}\sum_i \sum_j GLRLM(i,j) \cdot j^2$	Is highly dependent on the occurrence of long runs and is expected large for coarse textures.
Grey-Level Nonuniformity	$\frac{1}{n_r}\sum_i \left(\sum_j GLRLM(i,j)\right)^2$	Measures the similarity of grey level values throughout the image and is expected small if grey level values are similar throughout the image.
Run Length Nonuniformity	$\frac{1}{n_r}\sum_j \left(\sum_i GLRLM(i,j)\right)^2$	Measures the similarity of the length of runs throughout the image and is expected small if run lengths are similar throughout the image.
Run Percentage	$\frac{n_r}{n_p}$	Measures the heterogeneity and the distribution of runs of an image in a specific direction and is expected large for images with a heterogeneous texture.
Low Grey-Level Run Emphasis	$\frac{1}{n_r}\sum_i \sum_j \frac{GLRLM(i,j)}{i^2}$	Is highly dependent on the occurrence of runs with low grey levels.
High Grey-Level Run Emphasis	$\frac{1}{n_r}\sum_i \sum_j GLRLM(i,j) \cdot i^2$	Is highly dependent on the occurrence of runs with high grey levels.
Short Run Low Grey-Level Emphasis	$\frac{1}{n_r}\sum_i \sum_j \frac{GLRLM(i,j)}{i^2 \cdot j^2}$	Is highly dependent on the occurrence of short runs with low grey levels.
Short Run High Grey-Level Emphasis	$\frac{1}{n_r}\sum_i \sum_j \frac{GLRLM(i,j) \cdot i^2}{j^2}$	Is highly dependent on the occurrence of short runs with high grey levels.
Long Run Low Grey-Level Emphasis	$\frac{1}{n_r}\sum_i \sum_j \frac{GLRLM(i,j) \cdot j^2}{i^2}$	Is highly dependent on the occurrence of long runs with low grey levels.
Long Run High Grey-Level Emphasis	$\frac{1}{n_r}\sum_i \sum_j GLRLM(i,j) \cdot i^2 \cdot j^2$	Is highly dependent on the occurrence of long runs with high grey levels.

GLSZM-based second order textural features.

Notation:

$GLSZM(i,j)$	(i,j)th entry in a GLSZM.
$\sum_i GLSZM(i,j)$ and $\sum_j GLSZM(i,j)$	$\sum_{i=1}^{M} GLSZM(i,j)$ and $\sum_{j=1}^{N} GLSZM(i,j)$
n_r	$\sum_i \sum_j GLSZM(i,j)$
n_p	$\sum_i \sum_j j \cdot GSZLM(i,j)$

Variable	Equation	Description
Small Zone Emphasis	$\frac{1}{n_r}\sum_i \sum_j \frac{GLSZM(i,j)}{j^2}$	Is highly dependent on the occurrence of small zones and is expected large for fine textures.
Large Zone Emphasis	$\frac{1}{n_r}\sum_i \sum_j GLSZM(i,j) \cdot j^2$	Is highly dependent on the occurrence of large zones and is expected large for fine textures.
Grey-Level Nonuniformity	$\frac{1}{n_r}\sum_i \left(\sum_j GLSZM(i,j)\right)^2$	Measures the similarity of grey level values throughout the image and is expected small if grey level values are similar throughout the image.
Size Zone Nonuniformity	$\frac{1}{n_r}\sum_j \left(\sum_i GLSZM(i,j)\right)^2$	Measures the similarity of the length of runs throughout the image and is expected small if size zones are similar throughout the image.
Zone Percentage	$\frac{n_r}{n_p}$	Measures the heterogeneity and the distribution of size zones of an image in a specific direction and is expected large for images with a heterogeneous texture.
Low Grey-Level Zone Emphasis	$\frac{1}{n_r}\sum_i \sum_j \frac{GLSZM(i,j)}{i^2}$	Is highly dependent on the occurrence of zones with low grey levels.
High Grey-Level Zone Emphasis	$\frac{1}{n_r}\sum_i \sum_j GLSZM(i,j) \cdot i^2$	Is highly dependent on the occurrence of zones with high grey levels.
Small Zone Low Grey-Level Emphasis	$\frac{1}{n_r}\sum_i \sum_j \frac{GLSZM(i,j)}{i^2 \cdot j^2}$	Is highly dependent on the occurrence of small zones with low grey levels.
Small Zone High Grey-Level Emphasis	$\frac{1}{n_r}\sum_i \sum_j \frac{GLSZM(i,j) \cdot i^2}{j^2}$	Is highly dependent on the occurrence of small zones with high grey levels.
Large Zone Low Grey-Level Emphasis	$\frac{1}{n_r}\sum_i \sum_j \frac{GLSZM(i,j) \cdot j^2}{i^2}$	Is highly dependent on the occurrence of large zones with low grey levels.
Large Zone High Grey-Level Emphasis	$\frac{1}{n_r}\sum_i \sum_j GLSZM(i,j) \cdot i^2 \cdot j^2$	Is highly dependent on the occurrence of large zones with high grey levels.